JM PAPERS

Viscous effects on real gases in quasi-one-dimensional supersonic convergent divergent nozzle flows

Julián Restrepo[1],[†] and José R. Simões-Moreira[1]

[1]SISEA – Renewable and alternative Energy Systems Laboratory in the Mechl. Eng. Department at Escola Politécnica, Universidade de São Paulo, Av. Prof. Mello Moraes, 2231, 05508-900 São Paulo, SP, Brazil

Viscous effects on an ideal gas flow in a supersonic convergent–divergent nozzle are a well-studied subject in classical gas dynamics. However, the ideal assumption fails on fluids that exhibit complex behaviours such as near-critical-region and non-ideal dense vapours. Under those conditions, a realistic equation of state (EOS) plays a vital role for a precise and realistic computation. This work examines the problem for solving the quasi-one-dimensional viscous compressible flow using a realistic EOS. The governing equations are discretised and solved using the fourth-order Runge–Kutta method coupled with a state-of-the-art EOS to calculate the thermodynamic properties. The role of the Grüneisen parameter along with viscous and real gas effects and their influence on the sonic point formation are discussed. The study shows that the flow may not achieve the supersonic regime for any pressure ratio depending on the combination of that parameter and the normalised friction factor. In addition, the analysis yields the discharge coefficient and the isentropic nozzle efficiency, which may achieve maximum values as a function of the stagnation conditions. Finally, the study also evaluates the formation and intensity of normal shock waves by using the Rankine–Hugoniot relations, which now depend on the real gas and viscous effects in opposition to the inviscid solution. Moreover, the methodology used captures the sonic point and shock wave position by a space marching algorithm using the Brent method for scalar minimisation. Experimental data available in the open literature corroborate the approach.

Key words: gas dynamics, shock waves, supersonic flow

† Email addresses for correspondence: restrepo@usp.br, jcrestrepol@hotmail.com

1. Introduction

Convergent–divergent or de Laval nozzles are intensely studied devices because of their widespread application in industrial and aerospace industries. They are also used currently in several other processes such as carbon capture and storage (CCS) (Gernert & Span 2016) and the renewable energy field (Goodwin, Sengers & Peters 2010). Real gas effects have become more relevant within these applications, and using accurate equations of state (EOSs) has become a fundamental tool for precise and realistic flow calculations. In addition, current analysis is moving towards studying real gas mixtures in novel applications, such as organic Rankine cycles (ORCs) (Invernizzi *et al.* 2019), supersonic ejectors (Aidoun *et al.* 2019) and supersonic gas separators (Cao & Bian 2019). In view of that, this paper implements a multi-parameter EOS (MPEOS) for real single and mixture gas calculations because of their high reliability for pure (Colonna *et al.* 2006) and mixtures of real gases (Kunz & Wagner 2012), specifically at high pressures or near to the critical point (Span 2000), compared with more classical approaches as the cubic EOS.

In addition to the real gas effects, viscous effects may also be critical in some cases, especially for micro-nozzles (Louisos & Hitt 2012) or nozzles manufactured by alternative production methods (e.g. additive manufacturing) due to their inherent high surface roughness, leading to higher friction factors and consequently nozzle flow deviation from the isentropic behaviour.

As a general rule, a quasi-one-dimensional (quasi-1D) model is inaccurate for evaluating complex geometries or three-dimensional phenomena, because, this approach could not consider the flow properties gradients in the further dimensions. It is, however, a powerful tool to obtain a fast and surprisingly accurate insight into the problem as well as to identify the essential flow parameters. In addition, that model enables robust EOS implementation due to its lower computational cost, which explains its widespread use. Therefore, we give a brief introduction of the models developed for the real gas evaluation effects on supersonic nozzles.

Tsien (1946) was one of the pioneers in the evaluation of real gas supersonic flows: he used a Van der Walls EOS to compute the real gas effects on the flow and discussed the normal shock wave formation inside the nozzle. Later Johnson (1964) presented a numerical approach for real gas computation using the Beattie–Bridgeman EOS, comparing the ideal gas deviation with real gas outcomes. Thompson (1971*a*) explained the role of the fundamental derivative of gas dynamics on an inviscid nozzle and constant section duct with friction flows. Afterwards, Kluwick (1993) discussed the viscous and real gas interaction for a transonic nozzle, after using the small-perturbation technique and explored the non-classical fluid effects on the throat geometry and the shock-wave formation. Cramer & Fry (1993) used a similar approach for the evaluation of non-classical expansion in inviscid nozzles, and in a different work Cramer, Monaco & Fabeny (1994) evaluated the Fanno flows of non-ideal dense gases. In this same trend Schnerr & Leidner (1994) presented a rigorous evaluation of internal flows with multiple sonic points, which occurred in non-classical flows. Kluwick (2004) presented an evaluation of internal flows of dense gases, where he used two cases in his evaluation: an inviscid nozzle and laminar boundary-layer flows. Arina (2004) suggested a real gas model for a cubic EOS, including the well-known Van der Walls and Redlich–Kwong EOSs for solving the dense vapour region including the near to critical state. A shock-wave-capturing algorithm was implemented. In a different approach Cinnella & Congedo (2007) presented the viscous and real gas interaction on the dense gas flows. Guardone & Vimercati (2016) presented a

new formulation for the analytical solution of the convergent–divergent nozzle flow for a class of fluids known as Bethe–Zel'dovich–Thompson (BZT) fluids for several reservoir conditions in order to identify different operational regimes and at various shock-wave conditions. Raman & Kim (2018) presented a numerical solver for a convergent–divergent nozzle for carbon dioxide flow at supercritical conditions for different EOSs. Vimercati & Guardone (2018) showed a steady-state evaluation for real gas in nozzles and a shock-wave-capturing scheme for non-classical fluids with a high molecular complexity (BZT), using the Van der Waals EOS. Some authors devised accurate EOS simplifications for real gas applications, such as Sirignano (2018), who presented a new approach by introducing a linearisation procedure to a cubic EOS to extend its application to several gas dynamic problems, such as the convergent–divergent nozzle. In addition, Yeom & Choi (2019) proposed a novel approach using a stiffened gas EOS, in which the real gas EOS was simplified, being validated for perfect gas and liquid flows in nozzles, Tosto *et al.* (2021) present a rigorous analysis for dense vapours in compressible internal flows, such as an inviscid real gas nozzle and a real gas Fanno flow. Finally, Restrepo, Bolaños-Acosta & Simões-Moreira (2022) presented a methodology for applying the method of characteristics for pure and mixtures of real gases at non-ideal and supercritical flow conditions.

There exist several approaches for the solution and analysis of steady-state real gas compressible flow in nozzles as indicated previously. Nevertheless, the open literature lacks the evaluation of the real gas viscid effects on the sonic-point formation and the analysis of the viscous–real gas interaction effect on the nozzle performance. Most of previous works have focused on perfect gases flow, such as Hoffman (1969), who evaluated viscous effects on the nozzle performance (Mach number at the throat, discharge coefficient and nozzle efficiency), and the work presented by Beans (1970), whereby he proposed a methodology for solving generalised one-dimensional flow. In addition, Buresti & Casarosa (1989) analysed the one-dimensional adiabatic viscous flow of gas–particle equilibrium streams. Recently, Ferrari (2021*a*) presented analytical solutions for diabatic viscous one-dimensional flow and Ferrari (2021*b*) calculated the exact solution for the perfect gas compressible viscous flow for subsonic or supersonic conical nozzles. In a similar study Yeddula, Guzmán-Iñigo & Morgans (2022), presented an approach to solving the unsteady nozzle compressible flow with heat transfer using the Magnus expansion method.

Building up from previous analyses, this work presents a real gas formulation of compressible viscous flow and proposes a set of governing differential equations, which reveals the relationship between the real gas (through the Grüneisen parameter) and the friction factor. Furthermore, it is shown that at extreme operating conditions, namely high values of wall surface roughness and Grüneisen parameter in combination with small hydraulic diameter and low area ratio, the nozzle divergent part cannot achieve the supersonic regime for any pressure ratio. Finally, we discuss the stagnation condition effects on the unidimensional nozzle discharge coefficient C_d and the nozzle isentropic efficiency, η.

2. Compressible viscous real gas governing equations

Euler's equations for compressible flow were modified by introducing the wall viscous terms in the momentum equation according to Ferrari's formulation (Ferrari 2021*b*). Following the same approach, the conservation equations of mass, momentum and energy

for a quasi-1D adiabatic control volume are, respectively,

$$\frac{\partial(\rho A)}{\partial t} + \frac{\partial(\rho A V)}{\partial x} = 0, \tag{2.1}$$

$$\frac{\partial(\rho V A)}{\partial t} + \frac{\partial\left(PA + \rho V^2 A\right)}{\partial x} = -\pi \tau_w D_h + P\frac{\partial A}{\partial x}, \tag{2.2}$$

$$\frac{\partial}{\partial t}\left[\rho\left(e + \frac{V^2}{2}\right)A\right] + \frac{\partial}{\partial x}\left[\rho\left(e + \frac{V^2}{2}\right)VA\right] + \frac{\partial(PVA)}{\partial x} = 0, \tag{2.3}$$

where t is the time, x is the nozzle axis, A is the cross-section area, V is the flow velocity, P is pressure, τ_w is the wall friction shear stress, D_h is the hydraulic diameter, e is the specific internal energy and ρ is the density.

The Fanning friction factor f is defined by

$$f = \frac{\tau_w}{\frac{1}{2}\rho V^2}. \tag{2.4}$$

Introducing f in the momentum equation (2.2), and after evaluating (2.1)–(2.3) in a steady-state analysis, a non-conservative form is achieved, where h denotes the specific enthalpy:

$$\frac{1}{\rho}\frac{d\rho}{dx} + \frac{1}{V}\frac{dV}{dx} + \frac{1}{A}\frac{dA}{dx} = 0, \tag{2.5}$$

$$\frac{dP}{dx} + \rho V\frac{dV}{dx} = -\frac{2\rho V^2 f}{D_h}, \tag{2.6}$$

$$\frac{dh}{dx} + V\frac{dV}{dx} = 0. \tag{2.7}$$

In addition, after considering the Gibbs' relation

$$\frac{dh}{dx} = T\frac{ds}{dx} + \frac{1}{\rho}\frac{dP}{dx} + \sum_i \mu_i \frac{dN_i}{dx}, \tag{2.8}$$

where T, μ and s denote the temperature, chemical potential and specific entropy, respectively. After assuming a pure substance or a constant composition mixture $(dN_i/dx = 0)$ and substituting (2.8) into (2.7) and rearranging it, the energy equation becomes

$$T\frac{ds}{dx} + \frac{1}{\rho}\frac{dP}{dx} + V\frac{dV}{dx} = 0. \tag{2.9}$$

Finally, a system of ordinary differential equations (2.5), (2.6) and (2.9) is obtained, which governs the viscous compressible real gas flow. The solution of that system of equations requires their formulation in an explicit form.

To obtain that, let first the pressure $P(\rho, s)$, be formulated as an exact derivative

$$\frac{dP}{dx} = \left(\frac{\partial P}{\partial \rho}\right)_s \frac{d\rho}{dx} + \left(\frac{\partial P}{\partial s}\right)_\rho \frac{ds}{dx}. \tag{2.10}$$

Next, the Maxwell relations are introduced along with the definition of the Grüneisen parameter, this is a classical quantity used in real gas compressible flow analysis as studied

by Arp, Persichetti & Chen (1984), Menikoff & Plohr (1989) and Tosto *et al.* (2021) because this parameter represents the temperature and density slope in a logarithmic plane for an isentropic process, and is given by

$$Gr = \left(\frac{\partial \ln T}{\partial \ln \rho}\right)_s = \frac{\rho}{T}\left(\frac{\partial T}{\partial \rho}\right)_s \tag{2.11}$$

to obtain

$$\frac{\mathrm{d}\rho}{\mathrm{d}x} = \frac{1}{c^2}\left(\frac{\mathrm{d}P}{\mathrm{d}x} - Gr\rho T\frac{\mathrm{d}s}{\mathrm{d}x}\right), \tag{2.12}$$

where c is the speed of sound, after substituting (2.12) and (2.6) into (2.5), we obtain

$$\frac{1}{V}\frac{\mathrm{d}V}{\mathrm{d}x} + \frac{1}{A}\frac{\mathrm{d}A}{\mathrm{d}x} + \frac{1}{c^2}\left(-\frac{2V^2f}{D_h} - V\frac{\mathrm{d}V}{\mathrm{d}x} - GrT\frac{\mathrm{d}s}{\mathrm{d}x}\right) = 0, \tag{2.13}$$

in order to solve (2.13), the specific entropy increase rate in the nozzle has to be calculated; this is achieved after replacing (2.6) in (2.9) and rearranging it

$$\frac{\mathrm{d}s}{\mathrm{d}x} = \frac{2V^2f}{TD_h}. \tag{2.14}$$

After substituting (2.14) into (2.13) and some algebraic manipulation the velocity area relation is obtained for a real gas viscous compressible flow, where $M = V/c$ is the Mach number

$$\frac{\mathrm{d}V}{\mathrm{d}x} = \frac{\left(\dfrac{2f}{D_h}M^2(Gr+1) - \dfrac{1}{A}\dfrac{\mathrm{d}A}{\mathrm{d}x}\right)V}{\left(1 - M^2\right)}. \tag{2.15}$$

By analysing (2.15) one can note that Gr in association with the normalised friction factor f/D_h strongly affect the flow behaviour as it is analysed in detail further. Both contributions result in a new definition named the viscous potential, Π, given by

$$\Pi = \frac{2f}{D_h}(Gr+1), \tag{2.16}$$

which accounts for the departure from the isentropic flow formulation.

The Mach number variation inside the nozzle can be computed from (2.15) and by the Mach number definition and its differentiation, one achieves

$$\frac{1}{M}\frac{\mathrm{d}M}{\mathrm{d}x} = \frac{\Pi M^2 - \dfrac{1}{A}\dfrac{\mathrm{d}A}{\mathrm{d}x} - \dfrac{1}{c}\dfrac{\mathrm{d}c}{\mathrm{d}x}(1 - M^2)}{\left(1 - M^2\right)}. \tag{2.17}$$

The speed of sound derivative can be expressed explicitly as a function of pressure and specific entropy $c(P, s)$, which yields

$$\frac{\mathrm{d}c}{\mathrm{d}x} = \left(\frac{\partial c}{\partial P}\right)_s\frac{\mathrm{d}P}{\mathrm{d}x} + \left(\frac{\partial c}{\partial s}\right)_P\frac{\mathrm{d}s}{\mathrm{d}x}, \tag{2.18}$$

where, according to Thompson (1971*b*), the speed of sound partial derivatives can be formulated as follows:

$$\left(\frac{\partial c}{\partial P}\right)_s = \frac{\Gamma - 1}{\rho c}, \tag{2.19}$$

where Γ is the fundamental derivative of gas dynamics. It can be formulated as (Colonna *et al.* 2009)

$$\Gamma = 1 + \frac{\rho}{c}\left(\frac{\partial c}{\partial \rho}\right)_s \tag{2.20}$$

and

$$\left(\frac{\partial c}{\partial s}\right)_P = \rho c\left(\frac{\partial T}{\partial P}\right)_s + \frac{c^3\rho^2}{2}\left(\frac{\partial^2 T}{\partial P^2}\right)_s. \tag{2.21}$$

After several algebraic operations and thermodynamic definitions use, one can achieve

$$\left(\frac{\partial c}{\partial s}\right)_P = \frac{GrT}{c} + \frac{GrTc\rho}{2}\left(\left(\frac{\partial Gr}{\partial P}\right)_s \frac{1}{Gr} + \frac{Gr - 2\Gamma + 1}{\rho c^2}\right). \tag{2.22}$$

Finally, after substituting (2.19), (2.22) and (2.14) into (2.18), the speed of sound differential equation becomes

$$\frac{\mathrm{d}c}{\mathrm{d}x} = \frac{\Gamma - 1}{\rho c}\frac{\mathrm{d}P}{\mathrm{d}x} + \frac{GrM^2 fc}{D_h}\left(3 + \left(\frac{\partial Gr}{\partial P}\right)_s \frac{c^2\rho}{Gr} + Gr - 2\Gamma\right), \tag{2.23}$$

where

$$\left(\frac{\partial Gr}{\partial P}\right)_s = \frac{\rho}{T}\left(\frac{\partial^2 T}{\partial\rho\partial P}\right)_s + \frac{Gr(1 - Gr)}{\rho c^2}. \tag{2.24}$$

After inspecting (2.23) one can perceive that $\mathrm{d}c/\mathrm{d}x$ variation along the nozzle depends on the fluid's thermodynamic state measured by Γ, Gr, ρ, c and the flow conditions M, $\mathrm{d}P/\mathrm{d}x$ and f/D_h. Depending on the interaction of these parameters the speed of sound could behave in a non-ideal fashion.

After solving the velocity differential equation (2.15), it is possible to calculate the pressure (2.6), density (2.12) and specific enthalpy based on (2.8) to obtain

$$\frac{\mathrm{d}h}{\mathrm{d}x} = T\frac{\mathrm{d}s}{\mathrm{d}x} + \frac{1}{\rho}\frac{\mathrm{d}P}{\mathrm{d}x}. \tag{2.25}$$

In addition, the temperature $T(\rho, s)$ can be calculated by

$$\frac{\mathrm{d}T}{\mathrm{d}x} = \left(\frac{\partial T}{\partial\rho}\right)_s \frac{\mathrm{d}\rho}{\mathrm{d}x} + \left(\frac{\partial T}{\partial s}\right)_\rho \frac{\mathrm{d}s}{\mathrm{d}x}, \tag{2.26}$$

after some manipulation, where k is the isothermal compressibility and C_P is the specific heat at constant pressure, this yields

$$\frac{\mathrm{d}T}{\mathrm{d}x} = \frac{T}{\rho}\left(Gr\frac{\mathrm{d}\rho}{\mathrm{d}x} + \frac{k\rho^2 c^2}{C_P}\frac{\mathrm{d}s}{\mathrm{d}x}\right). \tag{2.27}$$

Note that for perfect gases the Grüneisen parameter becomes a function of γ, the isentropic expansion coefficient $Gr = \gamma - 1$. After substituting it into (2.14) and (2.15), this reproduces the perfect gas expression found in Zucrow (1976).

951 A14-6

2.1. *Sonic point*

It is noteworthy to mention that the sonic point is not located at the nozzle geometrical throat $\mathrm{d}A/\mathrm{d}x = 0$ for viscous flow being shifted to a location downstream of the throat in the divergent nozzle portion. This occurs due to the viscous effects on the flow (Hodge & Koenig 1995). For a more general situation (Beans 1970; Zucrow 1976), the sonic point is located where the numerator and denominator of (2.17) vanish simultaneously. Consequently, it leads to an indetermination of (2.17). At this point it is convenient to use the L'Hôpital's rule of calculus to obtain the solution, thus, after some algebraic manipulation, one obtains

$$\left(\frac{\mathrm{d}M}{\mathrm{d}x}\right)_{sonic} = -\frac{1}{2c}\frac{\mathrm{d}c}{\mathrm{d}x} - \frac{1}{2}\Pi \pm \frac{1}{2}\sqrt{\left(\Pi + \frac{1}{c}\frac{\mathrm{d}c}{\mathrm{d}x}\right)^2 - 2\frac{\mathrm{d}\Pi}{\mathrm{d}x} + \frac{2}{A}\frac{\mathrm{d}^2A}{\mathrm{d}x^2} - \frac{2}{A^2}\left(\frac{\mathrm{d}A}{\mathrm{d}x}\right)^2}. \tag{2.28}$$

After inspecting (2.28), the existence of two solutions is evident, which depends on the boundary conditions of the flow, being positive for the supersonic or negative for the subsonic solution, in the nozzle's divergent part.

2.2. *Sonic point displacement*

As examined in the last section, the sonic point location is conditioned by the Mach-area relationship (2.17), which leads to an indetermination as the fluid reaches the local speed of sound $M = 1$. Nevertheless, at some conditions the speed of sound may never be attained within the nozzle because of the combination of the following parameters: a high normalised friction factors f/D_h, a high Gr and a small area variation within the nozzle $\mathrm{d}A/\mathrm{d}x$. Their combined effects on the flow could be calculated by analytical methods after considering locally constant values of f and Gr for a nozzle geometry explicitly formulated as a function of x, i.e. $A = A(x)$. First, the sonic point can be calculated by finding the roots of (2.17) numerator by imposing the sonic condition given by $M^2 = 1$, which yields

$$\Pi = \frac{1}{A}\frac{\mathrm{d}A}{\mathrm{d}x}. \tag{2.29}$$

In order to present a study case, the Arina's nozzle geometry (Arina 2004) is analysed in non-dimensional coordinates, where L is the nozzle length and x_{th} is the geometric throat position, thus the nozzle's convergent section is expressed as

$$A(x) = 2.5 + 3\left(\frac{x}{x_{th}} - 1.5\right)\left(\frac{x}{x_{th}}\right)^2, \quad \text{for } L > x \leqslant x_{th}, \tag{2.30}$$

and the divergent section is

$$A(x) = 3.5 - \frac{x}{x_{th}}\left[6 - 4.5\frac{x}{x_{th}} + \left(\frac{x}{x_{th}}\right)^2\right], \quad \text{for } L > x \geqslant x_{th}. \tag{2.31}$$

Therefore, by substituting Arina's area dependence (2.31) into (2.29), and obtaining the solution, Π can be obtained for an x sonic point position given by

$$\Pi = \frac{3(x - 2x_{th})(x - x_{th})}{x^3 - 4.5x^2 x_{th} + 6x x_{th}^2 - 3.5x_{th}^3}. \tag{2.32}$$
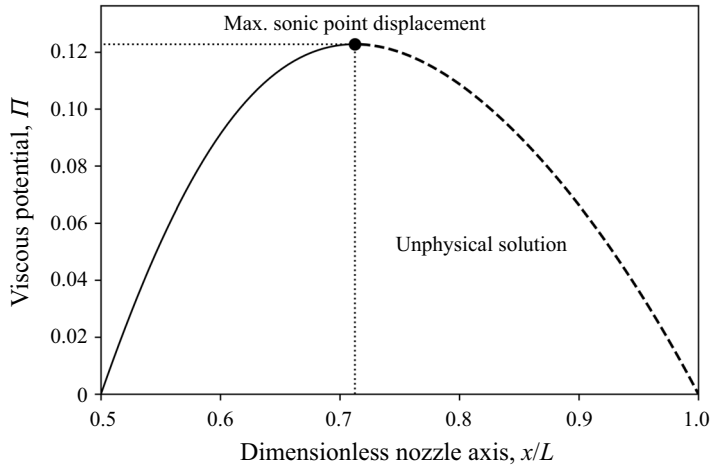
Figure 1. Viscous potential for a respective sonic point displacement, where the dashed line corresponds to the unphysical solution.

Figure 1 displays the viscous potential from (2.32) as a function of Arina's dimensionless axis x/L. By examining the graphics in that figure, one may observe that the sonic condition moves downstream up to $x/L = 0.712$ where the viscous potential is a maximum $\Pi = 0.123$. Beyond that position, the sonic point cannot be attained any longer within the nozzle. Mathematical solutions to the right of the maximum displacement sonic point (dashed line) do not have physical meaning.

For a more general nozzle, where $A(x)$ is known (2.33) displays a point of maximum for any geometry and viscous potential. That maximum condition is given the restriction that the x-derivative of (2.29) is null, which yields

$$\frac{\mathrm{d}(\Pi)}{\mathrm{d}x} = \frac{\mathrm{d}}{\mathrm{d}x}\left(\frac{1}{A}\frac{\mathrm{d}A}{\mathrm{d}x}\right) = 0, \tag{2.33}$$

after carrying out the derivative, one obtains

$$A\frac{\mathrm{d}^2A}{\mathrm{d}x^2} - \left(\frac{\mathrm{d}A}{\mathrm{d}x}\right)^2 = 0. \tag{2.34}$$

Hence, the solution of (2.34) gives the maximum sonic point displacement position x_{max}, which corresponds to the threshold of establishing a supersonic flow downstream of x_{max}. A higher Π will inhibit a supersonic flow from being attained. Taking Arina's nozzle geometry as an example, consider a high-pressure and low-temperature supercritical oxygen state ($Gr = 1.1$) and after employing (2.16) the maximum admissible f/D_h value is 0.029. In contrast, a low-pressure superheated oxygen exhibit a ($Gr = 0.38$), resulting in a maximum admissible f/D_h value of 0.044. Therefore, the maximum normalised friction factor will depend on the fluid thermodynamic state.

2.3. *Rankine–Hugoniot relations*

If the nozzle exit pressure is higher than the environment discharging pressure, but lower than the critical subsonic solution, a normal shock wave should be formed within the nozzle. The Rankine–Hugoniot relations (2.35)–(2.37) are widely known for the treatment

951 A14-8

of discontinuities on compressible flows (e.g. shock waves, detonations (Thompson 1971*b*) or even evaporation waves (Simões-Moreira & Shepherd 1999) and condensation shocks (Bolaños-Acosta, Restrepo & Simões-Moreira 2021)). The three conservation equations valid for a discontinuity are presented next, where the index 1 denotes the upstream state and 2 denotes the downstream state:

$$\rho_1 V_1 = \rho_2 V_2, \tag{2.35}$$

$$\rho_1 V_1^2 + P_1 = \rho_2 V_2^2 + P_2, \tag{2.36}$$

$$h_1 + \frac{1}{2} V_1^2 = h_2 + \frac{1}{2} V_2^2. \tag{2.37}$$

2.4. *Equation of state*

The MPEOS used in this work was formulated in terms of the specific Helmholtz free energy, using experimental data fitted by optimisation algorithms Span (2000). The classical definition of specific Helmholtz free energy is

$$a = e - Ts. \tag{2.38}$$

The MPEOS is based on the non-dimensional Helmholtz free energy $\alpha = a/(RT)$, where R is the universal gas constant. Here α can be calculated using the ideal α^0 and the residual part α^r. The residual part accounts for the real gas effects, and is calculated based on the polynomial, exponential and Gaussian bell-shaped terms corresponding to each substance,

$$\alpha = \alpha^0 + \alpha^r. \tag{2.39}$$

Once the ideal and residual parts of the non-dimensional Helmholtz free energy are calculated, any thermodynamic property can be calculated as a derivative of the Helmholtz free energy, using the relations defined by

$$\left.\begin{aligned}
\alpha_\delta^r = \left(\frac{\partial \alpha^r}{\partial \delta}\right)_\tau, \quad \alpha_{\delta\delta}^r = \left(\frac{\partial^2 \alpha^r}{\partial \delta^2}\right)_\tau, \quad \alpha_{\delta\tau}^r = \left(\frac{\partial^2 \alpha^r}{\partial \delta \partial \tau}\right), \\
\alpha_{\tau\tau}^o = \left(\frac{\partial^2 \alpha^\circ}{\partial \tau^2}\right)_\delta, \quad \alpha_{\tau\tau}^r = \left(\frac{\partial^2 \alpha^r}{\partial \tau^2}\right)_\delta,
\end{aligned}\right\} \tag{2.40}$$

where $\tau = T_c/T$ is the non-dimensional temperature and $\delta = \rho/\rho_c$ is the non-dimensional density. The Grüneisen parameter can be computed from the following definition, where β denotes the volume expansivity, which is derived from (2.11)

$$Gr = \frac{\beta c^2}{C_P}. \tag{2.41}$$

By substituting the definitions found in (2.40) into the non-dimensional Helmholtz free energy, one obtains

$$Gr = -\frac{\dfrac{1 + \delta\alpha_\delta^r - \delta\tau\alpha_{\delta\tau}^r}{1 + 2\delta\alpha_\delta^r + \delta^2\alpha_{\delta\delta}^r}\left(\dfrac{(1 + \delta\alpha_\delta^r - \delta\tau\alpha_{\delta\tau}^r)^2}{\tau^2\left(\alpha_{\tau\tau}^\circ + \alpha_{\tau\tau}^r\right)} - 1 - 2\delta\alpha_\delta^r - \delta^2\alpha_{\delta\delta}^r\right)}{\dfrac{\left(1 + \delta\alpha_\delta^r - \delta\tau\alpha_{\delta\tau}^r\right)^2}{1 + 2\delta\alpha_\delta^r + \delta^2\alpha_{\delta\delta}^r} - \tau^2\left(\alpha_{\tau\tau}^\circ + \alpha_{\tau\tau}^r\right)}. \tag{2.42}$$
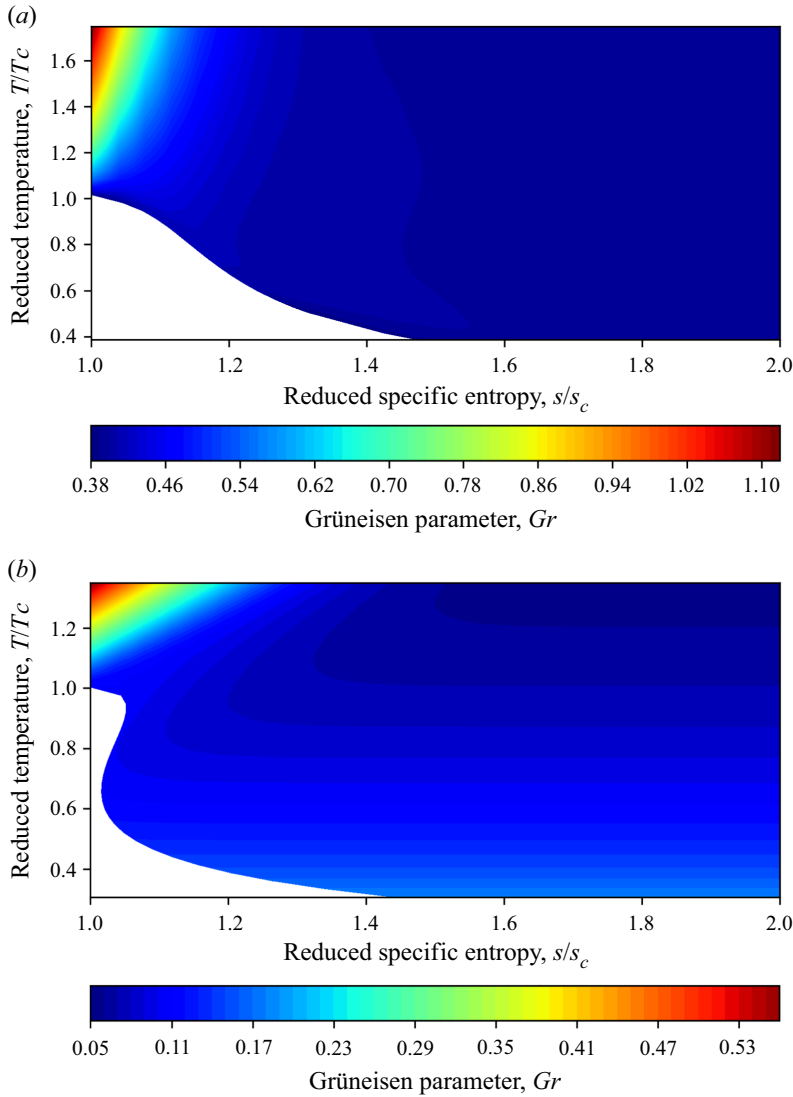
Figure 2. Grüneisen parameter variation for superheated and supercritical vapour of (*a*) oxygen and (*b*) isobutane.

Figure 2 presents the *Gr* behaviour in a reduced temperature–specific entropy plane, for an oxygen MPEOS (Schmidt & Wagner 1985) and for an isobutane EOS (Bücker & Wagner 2006) in superheated and supercritical phase, in addition, table 1 presents the thermodynamic properties (pressure, temperature and density) at the critical point for both evaluated fluids and the maximum operation pressure and temperature limits for each EOS. The figure shows the low variation of *Gr* for superheated vapours. That trend applies to both fluids. However, *Gr* steeply varies as the vapour phase becomes supercritical, especially for the region close to the critical point. A considerable difference can be perceived between both fluids due to their different molecular complexity, directly affecting the *Gr* calculation, because, as the fluid molecule becomes more complex (e.g. BZT fluids), the *Gr* value tends to decrease (Mausbach *et al.* 2016), and this directly affects

951 A14-10

Fluid	P_c (MPa)	T_c (K)	ρ_c (kg m^{-3})	P_{max} (MPa)	T_{max} (K)	EOS
Oxygen	5.04	154.58	436.14	80	2000	Schmidt & Wagner (1985)
Isobutane	3.63	407.82	225.50	35	575	Bücker & Wagner (2006)

Table 1. Critical properties and maximum pressure and temperature limits for oxygen and isobutane EOS.

the viscous effects on the nozzle. The dynamic viscosity for both pure substances were computed after using the work of Lemmon & Jacobsen (2004) and Vogel, Küchenmeister & Bich (2000) for the oxygen and isobutane, respectively.

2.5. *Friction factor*

The well-known Coolebrok–White equation was used to obtain the Darcy–Weisbach friction factor f_D, where ε denotes the channel surface roughness and *Re* is the Reynolds number:

$$\frac{1}{\sqrt{f_D}} = -2\log\left(\frac{\varepsilon}{3.7D_h} + \frac{2.51}{Re\sqrt{f_D}}\right). \tag{2.43}$$

Note that the Darcy–Weisbach friction factor is four times the Fanning friction factor $f = f_D/4$, and it is calculated for each computation step. The *Re* number of rectangular cross-section channels were computed using the methodology proposed by Jones (1976) for different aspect ratio geometries.

3. Numerical solution

The numerical solution scheme of the real viscous gas compressible flow and the shock-wave position is depicted in figure 3; this control volume is discretised using constant steps Δx. First, the sonic point location was found by the numerical root finding of (2.29) for the divergent nozzle part, where *Gr* and *f* values were initially computed for an isentropic sonic point located where $c(h_0, s_0) = V$. Next, the solution follows the HYBRD method (More, Garbow & Hillstrom 1980) for the root finding and this routine was implemented through SciPy libraries (Virtanen *et al.* 2020). After solving the sonic point, the algorithm uses the fourth-order Runge–Kutta method (RK-4) backwards until the nozzle inlet is reached. It was necessary to match the reservoir specific entropy s_0 to that from the solution obtained from the backwards RK-4 integration, because $s_{sonic} > s_0$ due to the entropy production (2.14), and this is performed through the s_{sonic} variation using the HYBRD method. After computing the specific entropy at the sonic point, the algorithm proceeded forward using RK-4 until the nozzle exit was found.

Note that for the sonic solution, $M = 1$, (2.15) cannot be solved as discussed in § 2.1, due to the indetermination of such an equation. Therefore, as the sonic point has been located, (2.28) was solved using a predictor–corrector finite difference scheme while $|M - 1| < 0.015$, for all the required derivatives and these equations were used to solve (2.28). This looping solution process continued until those derivatives matched the corresponding thermodynamic state after achieving a residual value from the last iteration less than 1×10^{-8}.

Flow thermodynamic properties (c, C_P, k, *Gr*) and dynamic viscosity were computed by using the code developed by Bell *et al.* (2014). In addition, a multidimensional solver
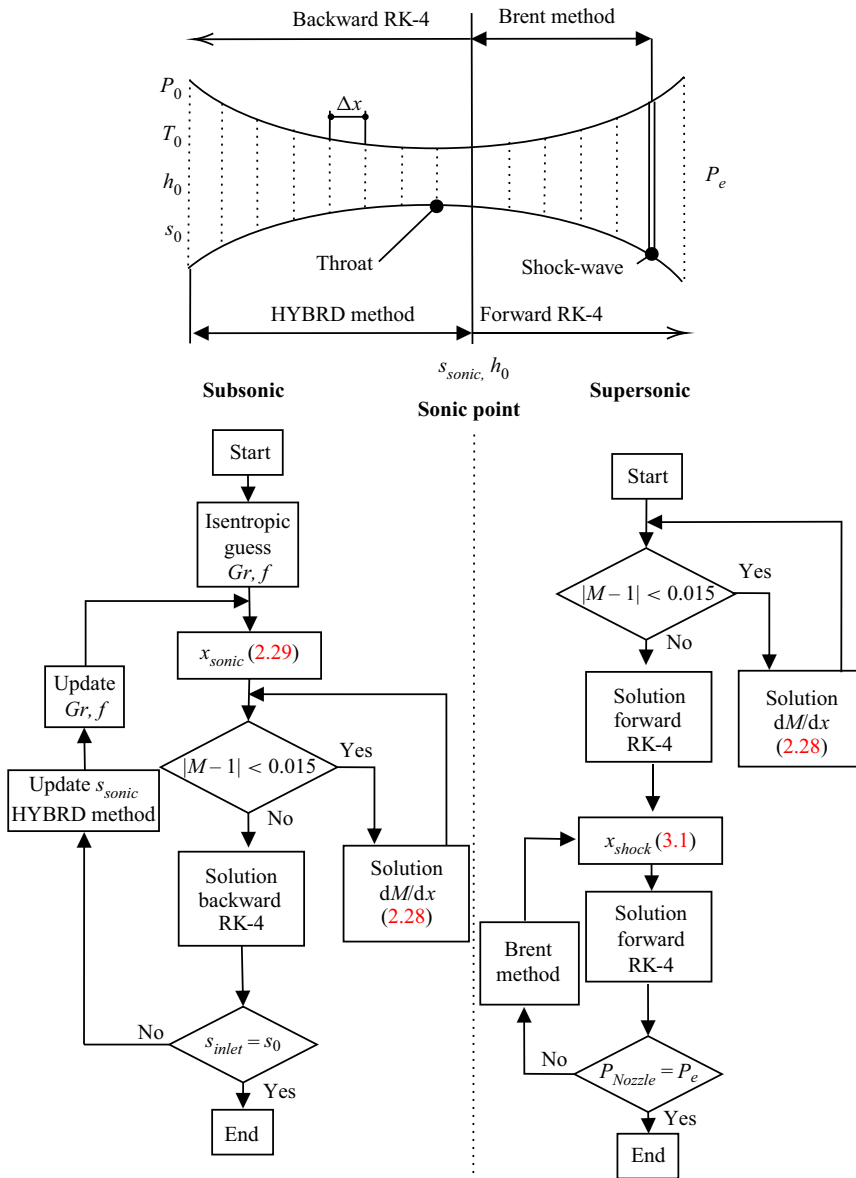
Figure 3. Numerical solution procedure.

was implemented using the HYBRD method for defining the thermodynamic state using specific enthalpy and specific entropy as independent variables (h, s). Specific entropy and enthalpy were computed using (2.14) and (2.25), respectively, for each calculation step. If there was a shock wave inside the nozzle, a new stagnation condition was calculated considering the shock-wave downstream conditions obtained after solving the Rankine–Hugoniot relations (2.35)–(2.37) by using the HYBRD method. However, the shock-wave position depends on the exit pressure; this was thus computed using the Brent method for minimising the following function:

$$g(x) = |P_{Nozzle} - P_e|, \tag{3.1}$$

951 A14-12
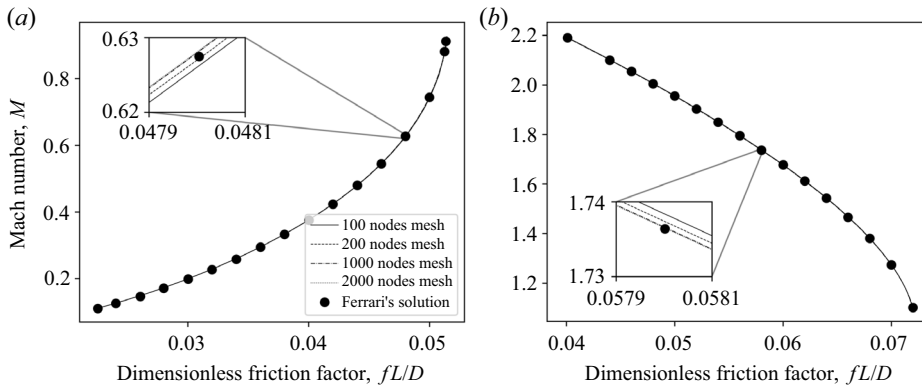
Figure 4. Ferrari (2021*b*) analytical and numerical results comparison: (*a*) subsonic and (*b*) supersonic solution.

where P_{nozzle} is the final nozzle pressure with a shock-wave position inside the nozzle and P_e is the exit pressure; therefore, the Brent minimisation method starts to march in space in the nozzle divergent part, seeking the condition whereby (3.1) is minimum after achieving a residual value from the last iteration less than 1×10^{-8}. It is important to highlight that the proposed method is devoted to solving non-ideal classical flows $\Gamma > 0$.

4. Results

4.1. *Validation and verification*

4.1.1. *Perfect viscous gas flow verification*

The first step in the proposed approach verification is to compare the developed methodology to the analytical viscous solution obtained by Ferrari (2021*b*). Ferrari's expression is developed for a viscid dilute gas in conical axisymmetric nozzles. Figure 4 presents the comparison outcomes for a different number of mesh nodes. Figure 4(*a*) is the subsonic solution obtained for the following conditions: $L = 45$ cm, initial diameter $D_1 = 8$ cm, final diameter $D_2 = 3.5$ cm, $P_0 = 5$ bar, $T_0 = 500$ K, $M_1 = 0.11$ and $f = 0.004$. Figure 4(*b*) is the supersonic solution obtained for the following conditions: $L = 60$ cm, initial diameter $D_1 = 5$ cm, final diameter $D_2 = 9$ cm, $P_0 = 2$ bar, $T_0 = 400$ K, $M_1 = 1.1$ and $f = 0.006$. These results are obtained after using the Lemmon *et al.* (2000) EOS. Figures 4(*a*) and 4(*b*) outcomes show the good performance of the developed method and display the mesh independence of the proposed numerical approach.

4.1.2. *Real viscous gas flow validation*

Table 2 presents the experimental data from open literature used for validating the proposed methodology. That table presents in the first column the tested fluid, followed by stagnation properties (P_0, T_0 and Z_0) used for each case with their respective references for the experimental data shown in the last column.

The experimental data reported by Spinelli *et al.* (2018) were used for the supersonic flow of octamethyltrisiloxane (MDM) (Thol *et al.* 2017), for the dynamic viscosity computation it was used the approach proposed by Klein, McLinden & Laesecke (1997). That substance has a high molecular weight ($M = 236.53$ g mol^{-1}) and, due to this high molecular weight and complexity, this substance exhibits a non-ideal compressible behaviour near to the critical point. Considering the stagnation conditions presented in

Fluid	P_0 (bar)	T_0 (K)	Z_0	Experiment
MDM	9.20	540.7	0.63	Spinelli *et al.* (2018)
Water	100.7	703.15	0.82	Gyarmathy (2005)
75 % CO_2–air mixture	9.98	265.2	0.94	Bier, Ehrler & Niekrawietz (1990)

Table 2. Stagnation points and experimental data used for validation.

table 2, a numerical simulation was performed for a 750 uniformly spaced element mesh. Figure 5(*a*) presents the numerical simulation for the pressure profile. Figure 5(*b*) presents the Mach number comparison against the experimental results. Good agreement was found between the simulation and the experimental results. For the last pressure measurement, the deviation reached 7.2 %. In addition, the numerical simulation performed by Gori *et al.* (2020) was used to compare the MDM results with a multidimensional computational fluid dynamics (CFD) solver. After comparing the numerical outcome with the experimental data and the multidimensional solver, it was found that the proposed approach presents a good solution and the Mach number profile results represent the trend of the experimental outcomes.

The EOS of Wagner & Pruß (2002) was used for the high-pressure steam simulation and the 4B nozzle of Gyarmathy (2005) was simulated using a 750-element mesh, which was found to be stable and mesh size independent. The approach of Huber *et al.* (2009) was used for the dynamic viscosity estimation. High deviations in pressure (13.6 %) were found in this simulation for low supersonic Mach numbers; otherwise the simulation gave better results as the viscous effects became more relevant at the nozzle outlet where the pressure deviation fell (to 4.6 %).

For the mixture validation, the experimental data of Bier *et al.* (1990) were used for a mixture of carbon dioxide and atmospheric dry air. For the sake of simplicity air was treated as pure nitrogen using the GERG-2008 MPEOS (Kunz & Wagner 2012). The formulation of Wilke (1950) was used for the mixture dynamic viscosity calculation. Table 2 presents the stagnation conditions of the test, and figure 5(*d*) presents the pressure profile comparison between the experimental and simulation for a 500-element mesh.

Note that the dynamic viscosity computation has an important role in the solution. Nevertheless, not all fluids have dedicated models for their estimation, as in the MDM case. Therefore, the dynamic viscous model selection could be relevant on the model performance.

4.1.3. *Shock-wave position verification*

For the shock-wave model capturing verification, the same work by Arina (2004) was used due to its benchmark widespread use in supersonic nozzles flows. The MPEOS was used for air and nitrogen mixtures (Lemmon *et al.* 2000).

Figure 6 presents the nozzle pressure profile; the solution obtained by Arina (2004) was compared reproducing precisely the pressure jump and shock location.

4.2. *Viscous effects on flow*

The next set of analyses of the viscous effects on the Arina's nozzle is to compare the isentropic flow at the same stagnation conditions and nozzle geometry. Figure 7 presents the results for the supersonic expansion of two substances oxygen and isobutane
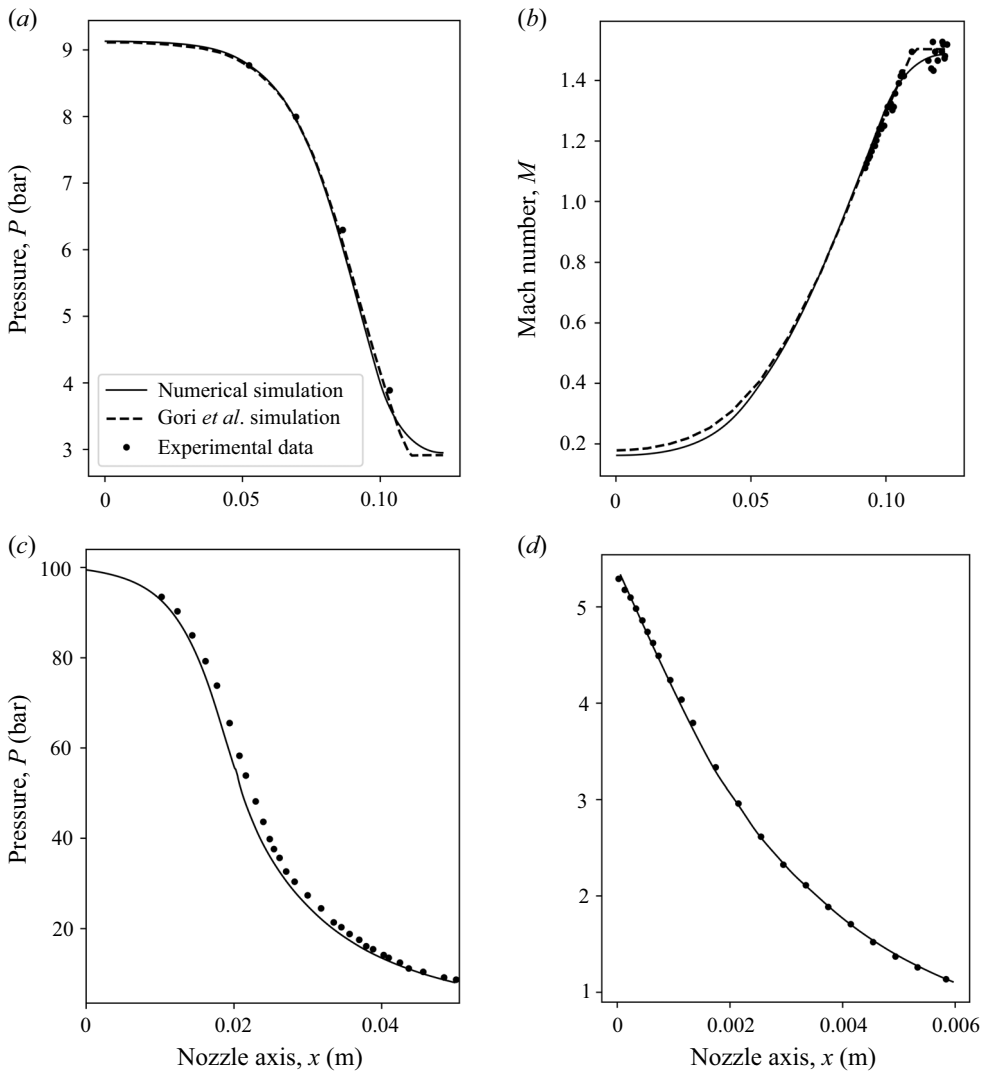
951 A14-14

Figure 5. Experimental results used for validation: (*a*) pressure profile and (*b*) Mach profile MDM; (*c*) pressure profile for water; (*d*) pressure profile for 75 % CO_2–air mixture; the black continuous line represents the numerical solution and the black solid points, the experimental data.

for a stagnation pressure and temperature of (13.9 MPa, 240 K) and (10 MPa, 520 K), respectively. Resulting in the same reduced pressure for both cases $P_r = P/P_c = 2.75$. The stagnation temperature of the isobutane case was selected to display the fluid's non-ideal behaviour in the supersonic expansion; on the other hand, the oxygen case stagnation temperature was chosen to avoid the two-phase region achievement at the nozzle outlet.

Both nozzles follow Arina geometrical design having the following geometric parameters: $x_{th} = 0.05$ m, $L = 0.1$ m, $D_{th} = 2 \times 10^{-3}$ m, $\epsilon = 1 \times 10^{-6}$ m and a 1200-element mesh, obtained after ensuring a grid-independent result. Those parameters lead to small dA/dx, D_h and a high f, resulting in a high viscous effect. In the presented numerical examples, the viscous potential plays an important role in the supersonic expansion leading to a maximum point for the four evaluated variables (P, M, c, Gr) and for both fluids. This
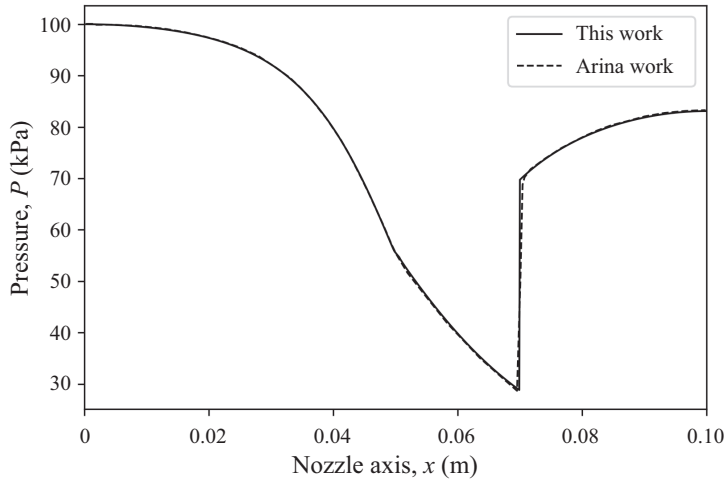
Figure 6. Pressure distribution Arina's nozzle ($P_0 = 100$ kPa, $T_0 = 288$ K) for dry air.

point results from the effects of the viscous potential on the velocity potential as seen in (2.15), and as Π exceeds the area change rate, the velocity decreases and this leads to a change in all thermodynamics properties. For all figure 7 outcomes, the blue shaded region represents the viscid solution's departure from the isentropic solution.

4.2.1. *Viscous effects on pressure profile*

As presented before, the viscous effects are relevant and the nozzle behaviour departs from the isentropic flow as presented in figures 7(*a*) and 7(*b*) for the isobutane and oxygen pressure profile. The isobutane case achieved a slighter higher normalised friction factor f/D_h at the sonic point; nevertheless, the oxygen case deploys a higher Gr value on the nozzle, resulting in an important change in the pressure profile. That occurs in part because of the change in the velocity potential as explained previously. In addition, the pressure profile shifts compared with the isentropic results due to the ds/dx increase, and this can be computed by substituting (2.14) into (2.10), resulting in $2Gr\rho V^2 f/D_h$. Therefore, the pressure profile shift is always positive and strongly influenced by the fluid velocity as seen in the deviation area in the pressure profiles in figures 7(*a*) and 7(*b*). Finally, if $Gr \to 0$, the pressure profile is closer to the isentropic profile as shown in figure 7(*a*) for isobutane, because isobutane has $Gr = 0.088$ at the sonic point compared with $Gr = 0.47$ for oxygen.

4.2.2. *Viscous effects on Mach number*

Analogously, figures 7(*c*) and 7(*d*) present the viscous effects on the Mach profile and their corresponding maximum points. Even though oxygen has a higher Gr, value at the sonic point compared with isobutane Gr; the sonic offset slightly changes for both fluids as can be seen in figures 7(*c*) and 7(*d*). In addition, the viscous effects lead to a decrease of the nozzle mass flow rate as a consequence of the sonic point shift.

4.2.3. *Viscous effects on flow speed of sound*

Finally, figures 7(*e*) and 7(*f*) present the speed of sound profile within the nozzle. The isobutane plot shows a non-monotonic behaviour, exhibiting the minimum and maximum
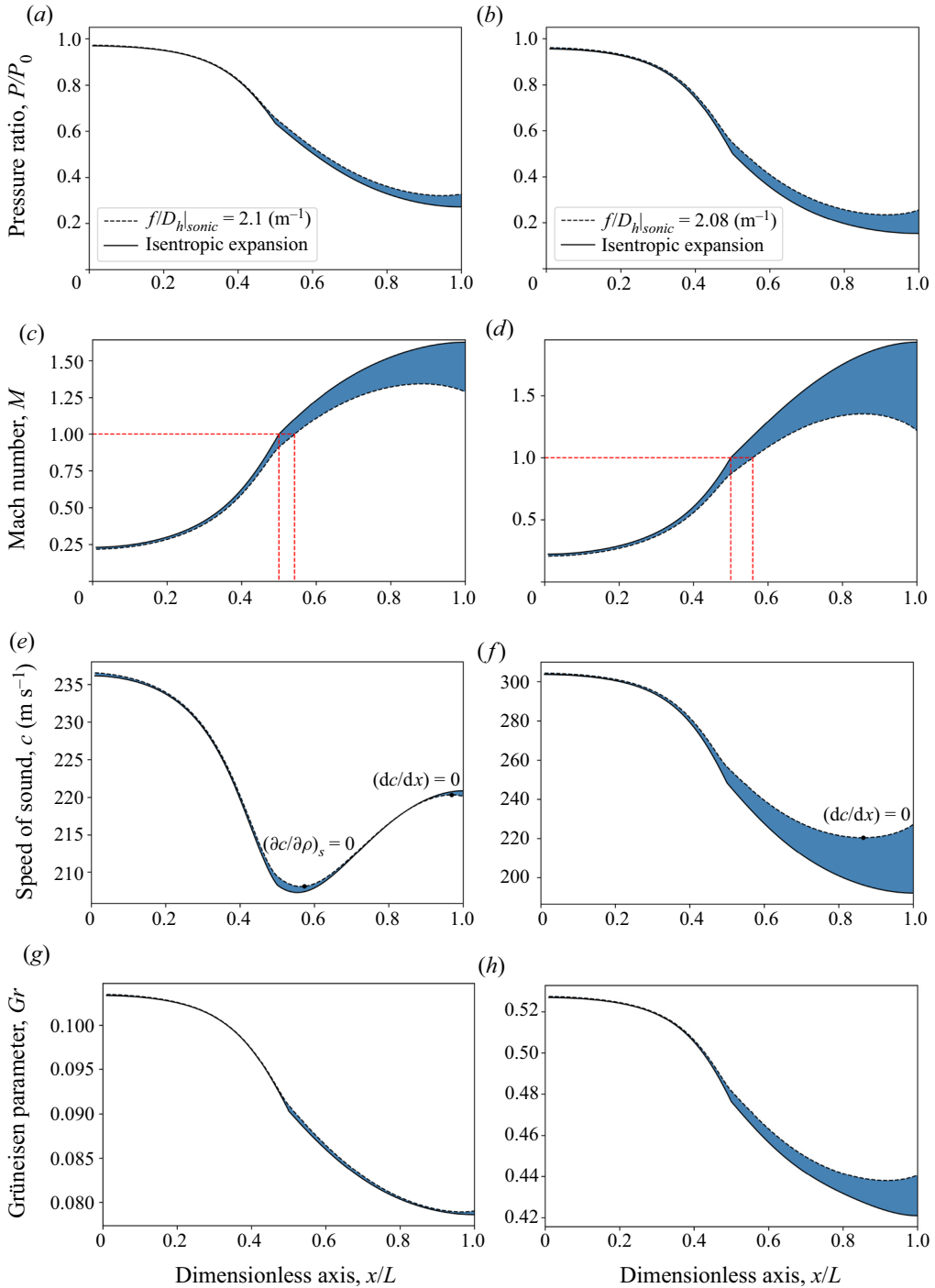
951 A14-16

Figure 7. Nozzle viscous effects, where simulations on the left correspond to isobutane and those on the right correspond to oxygen: (*a,b*) Pressure profile; (*c,d*) the Mach profile; (*e,f*) speed of sound profile on the nozzle; (*g,h*) Grüneisen parameter profile on the nozzle. Black continuous lines represent the isentropic expansion and dashed lines represent the viscous solution.

points; the minimum point occurs due to the expansion of non-ideal gas behaviour represented by $(\partial c/\partial \rho)_s = 0$. Therefore, the fluid expands into the non-ideal region, leading to an increase in the speed of sound until that the next maximum point is achieved due to the viscous effects. Thus, the speed of sound exhibits various inflexions points due to the combined effect of their non-ideal behaviour and the viscous effects as expected after inspecting (2.23). In addition, figures 7(*e*) and 7(*f*) show the difference in the speed of sound deviation between the isentropic and the viscid solution, because the offset for the oxygen case is considerably more evident than the isobutane due to the viscous effects on the last term of (2.23), so as $Gr \to 0$ the speed of sound profile will be closer to the isentropic solution.

4.2.4. *Viscous effects on the Grüneisen parameter*

As stressed out in the last sections the isobutane case presents lower Gr values than the oxygen case, and this originates a strong departure of the viscous solution after comparing both fluids. Even though the isobutane presents a non-ideal behaviour the Grüneisen parameter behaves in a similar fashion (figure 7*g*) to the oxygen case (figure 7*h*). However, the deviation of the viscous profile is more intense in the oxygen case than in the isobutane case.

4.2.5. *Viscous effects on shock-wave intensity and position*

Figure 8 presents the viscous effects on the intensity and shock-wave position for oxygen at the following stagnation conditions: (13.9 MPa, 240 K) employing an Arina nozzle with the following geometric parameters $x_{th} = 0.05$ m, $L = 0.1$ m, $D_{th} = 4 \times 10^{-3}$ m and three different values of surface roughness height ($\epsilon = 1 \times 10^{-7}$ m, 1×10^{-6} m, 1×10^{-5} m) and an isentropic expansion for a 1200-element mesh. As presented in figure 8(*a*), all the simulations converge on the same exit pressure $0.72 \times P_0$. Nevertheless, the pressure profile varies due to the viscous effects, because as long as the f/D_h increases the shock-wave intensity decreases due to the Mach number reduction, leading to a small entropy increment by the shock wave. However, the viscous effects over the total specific entropy jump in the nozzle is stronger as the f/D_h increases.

4.3. *Nozzle performance*

The analysis proposed allows important supersonic nozzle parameters to be calculated, i.e. discharge coefficient C_d,

$$C_d = \frac{\dot{m}_{viscous}}{\dot{m}_{iso}}, \tag{4.1}$$

and nozzle efficiency η,

$$\eta = \frac{h_0 - h_e}{h_0 - h_s}. \tag{4.2}$$

The discharge coefficient captures the viscous effects over the ideal mass flow rate from a quasi-1D perspective, and the nozzle efficiency compares the actual kinetic energy at the nozzle exit against the kinetic energy corresponding to an isentropic expansion at the same exit pressure. Nevertheless, this works gives novel insights into the real gas effects on the nozzle performance. Figure 9 presents the effect of the stagnation condition on the C_d and η values, for the following geometric variables for the Arina nozzle: $x_{th} = 0.05$ m, $L = 0.1$ m, $D_{th} = 4 \times 10^{-3}$ m and $\epsilon = 1 \times 10^{-6}$ m for the 1200-uniformly-spaced-element
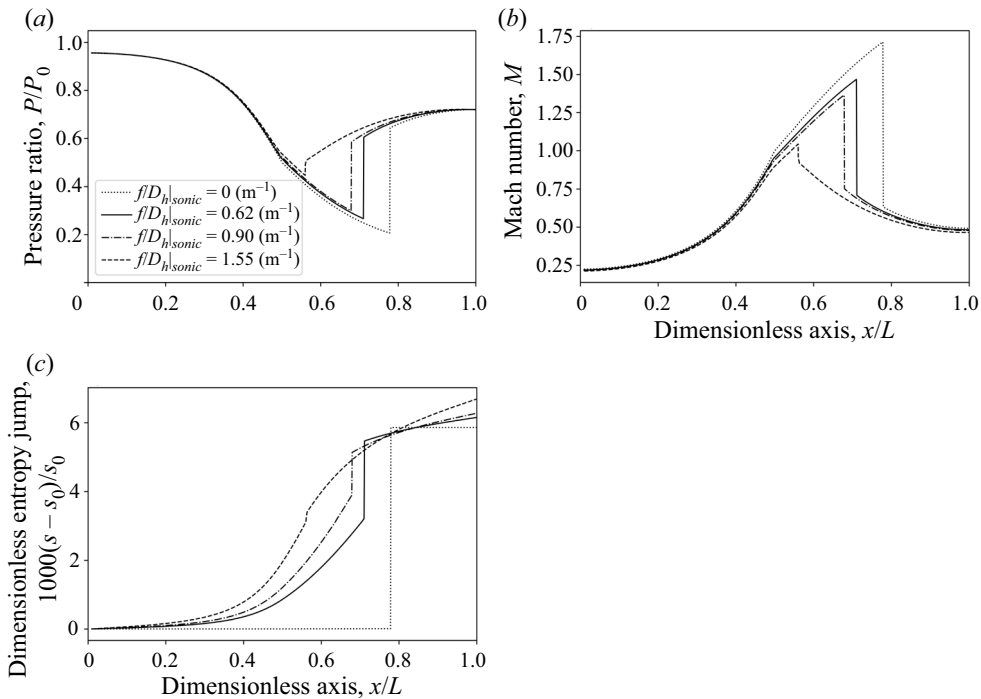
951 A14-18

Figure 8. Viscous effects on the shock-wave formation for oxygen: (*a*) pressure profile, (*b*) Mach profile and (*c*) dimensionless specific entropy jump in the nozzle.

mesh. Figures 9(*a*) and 9(*b*) show the C_d and η results for oxygen. These outcomes were obtained for several reduced stagnation pressures P_0/P_c and temperatures T_0/T_c. Both variables have low values at low pressures due to the low Re value and their subsequently high f in such conditions and, as the pressure increases, the C_d and η reach their maximum value due to the Re increase. However, if the pressure continues growing the nozzle performance decreases. This occurs due to the behaviour of the Gr and its effect on the viscous effects; as can be seen in figure 2 the Grüneisen parameter increases in the supercritical region close to the critical point. In addition, after comparing figures 9(*a*)–9(*c*), it is possible to observe the inverse relationship between the nozzle performance and the viscous potential, because Π shows the connection between the real and the viscous effects. Finally, figure 9(*d*) shows the compressibility factor outcome for the nozzles evaluated. Note that the simulations performed covered wide Z values and the viscous potential is almost insensitive to such changes.

5. Conclusions

This work has presented a new real gas model for computing the viscous effects on convergent–divergent supersonic flows. The new formulation reveals the role of the Grüneisen parameter in the viscous flow; this model has been integrated with modern EOSs to achieve accurate results and even consider the non-ideal or supercritical effects on the flow. Moreover, this approach can be used for pure substances and for constant composition gas mixtures as long as they remain in the gas phase. This model has been validated against experimental data, leading to a good agreement for all the cases calculated.
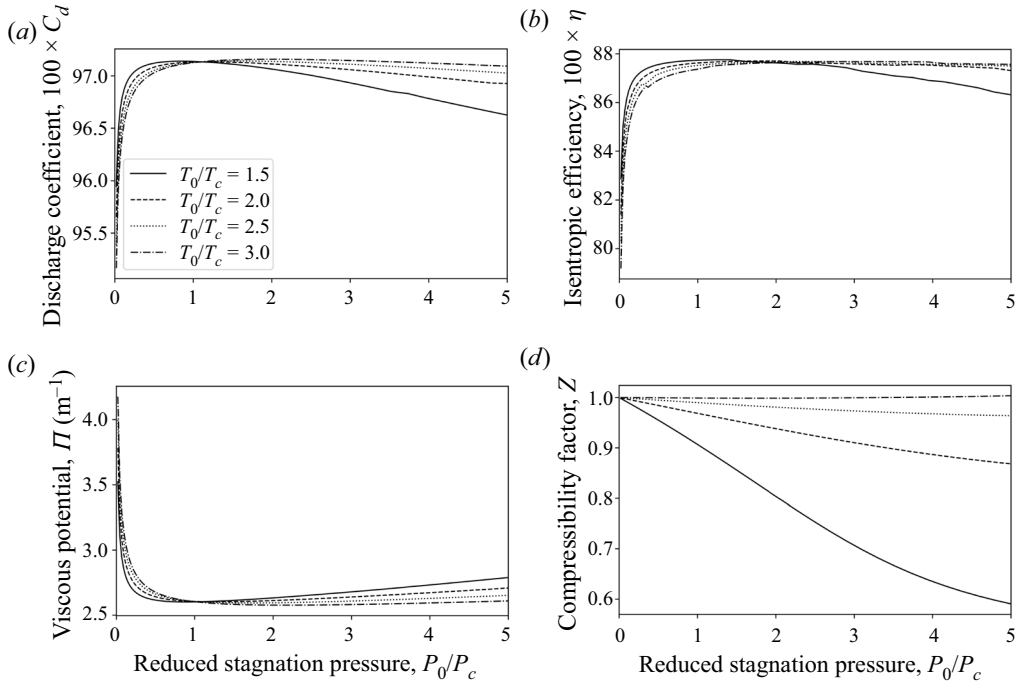
Figure 9. Nozzle performance for a supersonic oxygen nozzle: (*a*) C_d, (*b*) η, (*c*) viscous potential at nozzle sonic point and (*d*) compressibility factor.

Viscous effects on the sonic point formation have been studied showing that as the viscous potential increases, the sonic point moves towards to nozzle exit section. However, if the viscous potential achieves its maximum value, the nozzle does not reach the supersonic regime for any pressure ratio. Finally, it has been shown that for locally constant Gr, f values, the maximum viscous potential will be a function of the nozzle geometry.

Viscous effects may be strong enough to influence the velocity relation and invert their behaviour; this condition affects the flow thermodynamic properties (i.e. temperature, pressure and density). For non-ideal flows, viscous effects give additional inflexion points compared with an inviscid analysis. In addition, it was shown that the viscous potential affects the shock-wave position and strength.

The nozzle performance measured by its isentropic efficiency and discharge coefficient is highly dependent on the viscous potential, and due to the viscous and real gas effects, the nozzle performance achieves a maximum value for a certain stagnation condition and as the real gas effects (measured through the Gr) increases or the Re decreases the overall performance decreases.

Declaration of interests. The authors report no conflicts of interest.

Author ORCIDs.

Julián Restrepo https://orcid.org/0000-0003-3519-5744;

José R. Simões-Moreira https://orcid.org/0000-0002-8071-8420.

951 A14-20

References

AIDOUN, Z., AMEUR, K., FALSAFIOON, M. & BADACHE, M. 2019 Current advances in ejector modeling, experimentation and applications for refrigeration and heat pumps. Part 1: single-phase ejectors. *Inventions* **4** (1), 15.

ARINA, R. 2004 Numerical simulation of near-critical fluids. *Appl. Numer. Maths* **51** (4), 409–426.

ARP, V., PERSICHETTI, J.M. & CHEN, G.-B. 1984 The Grüneisen parameter in fluids. *Trans. ASME J. Fluids Engng* **106** (2), 193–200.

BEANS, E.W. 1970 Computer solution to generalized one-dimensional flow. *J. Spacecr. Rockets* **7** (12), 1460–1464.

BELL, I.H., WRONSKI, J., QUOILIN, S. & LEMORT, V. 2014 Pure and pseudo-pure fluid thermophysical property evaluation and the open-source thermophysical property library COOLPROP. *Ind. Engng Chem. Res.* **53** (6), 2498–2508.

BIER, K., EHRLER, F. & NIEKRAWIETZ, M. 1990 Experimental investigation and computer analysis of spontaneous condensation in stationary nozzle flow of CO_2-air mixtures. In *Adiabatic Waves in Liquid-Vapor Systems* (ed. G.E.A. Meier & P.A. Thompson), pp. 113–127. Springer.

BOLAÑOS-ACOSTA, A.F., RESTREPO, J.C. & SIMÕES-MOREIRA, J.R. 2021 Two semi-analytical approaches for solving condensation shocks in supersonic nozzle flows. *Intl J. Heat Mass Transfer* **173**, 121212.

BÜCKER, D. & WAGNER, W. 2006 Reference equations of state for the thermodynamic properties of fluid phase n-butane and isobutane. *J. Phys. Chem. Ref. Data* **35** (2), 929–1019.

BURESTI, G. & CASAROSA, C. 1989 One-dimensional adiabatic flow of equilibrium gas–particle mixtures in long vertical ducts with friction. *J. Fluid Mech.* **203**, 251–272.

CAO, X. & BIAN, J. 2019 Supersonic separation technology for natural gas processing: a review. *Chem. Engng Process. Process. Intensif.* **136**, 138–151.

CINNELLA, P. & CONGEDO, P.M. 2007 Inviscid and viscous aerodynamics of dense gases. *J. Fluid Mech.* **580**, 179–217.

COLONNA, P., NANNAN, N.R., GUARDONE, A. & LEMMON, E.W. 2006 Multiparameter equations of state for selected siloxanes. *Fluid Phase Equilib.* **244** (2), 193–211.

COLONNA, P., NANNAN, N.R., GUARDONE, A. & VAN DER STELT, T.P. 2009 On the computation of the fundamental derivative of gas dynamics using equations of state. *Fluid Phase Equilib.* **286** (1), 43–54.

CRAMER, M.S. & FRY, R.N. 1993 Nozzle flows of dense gases. *Phys. Fluids* A **5** (5), 1246–1259.

CRAMER, M.S., MONACO, J.F. & FABENY, B.M. 1994 Fanno processes in dense gases. *Phys. Fluids* **6** (2), 674–683.

FERRARI, A. 2021*a* Analytical solutions for one-dimensional diabatic flows with wall friction. *J. Fluid Mech.* **918**, A32.

FERRARI, A. 2021*b* Exact solutions for quasi-one-dimensional compressible viscous flows in conical nozzles. *J. Fluid Mech.* **915**, A1.

GERNERT, J. & SPAN, R. 2016 EOS–CG: a Helmholtz energy mixture model for humid gases and CCS mixtures. *J. Chem. Thermodyn.* **93**, 274–293.

GOODWIN, A.R., SENGERS, J. & PETERS, C.J., ed. 2010 *Applied Thermodynamics of Fluids*. Royal Society of Chemistry.

GORI, G., ZOCCA, M., CAMMI, G., SPINELLI, A., CONGEDO, P.M. & GUARDONE, A. 2020 Accuracy assessment of the non-ideal computational fluid dynamics model for siloxane MDM from the open-source SU2 suite. *Eur. J. Mech. B/Fluids* **79**, 109–120.

GUARDONE, A. & VIMERCATI, D. 2016 Exact solutions to non-classical steady nozzle flows of Bethe–Zel'dovich–Thompson fluids. *J. Fluid Mech.* **800**, 278–306.

GYARMATHY, G. 2005 Nucleation of steam in high-pressure nozzle experiments. *Proc. Inst. Mech. Engrs* A **219** (6), 511–521.

HODGE, B.K. & KOENIG, K. 1995 *Compressible Fluid Dynamics with Personal Computer Applications*. Prentice Hall.

HOFFMAN, J.D. 1969 Approximate analysis of nonisentropic flow in conical nozzles. *J. Spacecr. Rockets* **6** (11), 1329–1334.

HUBER, M.L., PERKINS, R.A., LAESECKE, A., FRIEND, D.G., SENGERS, J.V., ASSAEL, M.J., METAXA, I.N., VOGEL, E., MAREŠ, R. & MIYAGAWA, K. 2009 New international formulation for the viscosity of H_2O. *J. Phys. Chem. Ref. Data* **38** (2), 101–125.

INVERNIZZI, C.M., AYUB, A., DI MARCOBERARDINO, G. & IORA, P. 2019 Pure and hydrocarbon binary mixtures as possible alternatives working fluids to the usual organic Rankine cycles biomass conversion systems. *Energies* **12** (21), 4140.

JOHNSON, R.C. 1964 Calculations of real-gas effects in flow through critical-flow nozzles. *Trans. ASME J. Basic Engng* **86** (3), 519–525.

JONES, O.C. 1976 An improvement in the calculation of turbulent friction in rectangular ducts. *Trans. ASME J. Fluids Engng* **98** (2), 173–180.

KLEIN, S.A., MCLINDEN, M.O. & LAESECKE, A. 1997 An improved extended corresponding states method for estimation of viscosity of pure refrigerants and mixtures. *Intl J. Refrig.* **20** (3), 208–217.

KLUWICK, A. 1993 Transonic nozzle flow of dense gases. *J. Fluid Mech.* **247**, 661–688.

KLUWICK, A. 2004 Internal flows of dense gases. *Acta Mech.* **169** (1), 123–143.

KUNZ, O. & WAGNER, W. 2012 The GERG-2008 wide-range equation of state for natural gases and other mixtures: an expansion of GERG-2004. *J. Chem. Engng Data* **57** (11), 3032–3091.

LEMMON, E.W. & JACOBSEN, R.T. 2004 Viscosity and thermal conductivity equations for nitrogen, oxygen, argon, and air. *Intl J. Thermophys.* **25** (1), 21–69.

LEMMON, E.W., JACOBSEN, R.T., PENONCELLO, S.G. & FRIEND, D.G. 2000 Thermodynamic properties of air and mixtures of nitrogen, argon, and oxygen from 60 to 2000 K at Pressures to 2000 MPa. *J. Phys. Chem. Ref. Data* **29** (3), 331–385.

LOUISOS, W.F. & HITT, D.L. 2012 Viscous effects on performance of two-dimensional supersonic linear micronozzles. *J. Spacecr. Rockets* **45**, 706–715.

MAUSBACH, P., KÖSTER, A., RUTKAI, G., THOL, M. & VRABEC, J. 2016 Comparative study of the Grüneisen parameter for 28 pure fluids. *J. Chem. Phys.* **144** (24), 244505.

MENIKOFF, R. & PLOHR, B.J. 1989 The Riemann problem for fluid flow of real materials. *Rev. Mod. Phys.* **61** (1), 75–130.

MORE, J.J., GARBOW, B.S. & HILLSTROM, K.E. 1980 User guide for MINPACK-1 [in Fortran].

RAMAN, S.K. & KIM, H.D. 2018 Solutions of supercritical CO_2 flow through a convergent–divergent nozzle with real gas effects. *Intl J. Heat Mass Transfer* **116**, 127–135.

RESTREPO, J.C., BOLAÑOS-ACOSTA, A.F. & SIMÕES-MOREIRA, J.R. 2022 Short nozzles design for real gas supersonic flow using the method of characteristics. *Appl. Therm. Engng* **207**, 118063.

SCHMIDT, R. & WAGNER, W. 1985 A new form of the equation of state for pure substances and its application to oxygen. *Fluid Phase Equilib.* **19** (3), 175–200.

SCHNERR, G.H. & LEIDNER, P. 1994 Internal flows with multiple sonic points. In *Fluid- and Gasdynamics*, pp. 147–154. Springer.

SIMÕES-MOREIRA, J.R. & SHEPHERD, J.E. 1999 Evaporation waves in superheated dodecane. *J. Fluid Mech.* **382**, 63–86.

SIRIGNANO, W.A. 2018 Compressible flow at high pressure with linear equation of state. *J. Fluid Mech.* **843**, 244–292.

SPAN, R. 2000 *Multiparameter Equations of State*. Springer.

SPINELLI, A., CAMMI, G., GALLARINI, S., ZOCCA, M., COZZI, F., GAETANI, P., DOSSENA, V. & GUARDONE, A. 2018 Experimental evidence of non-ideal compressible effects in expanding flow of a high molecular complexity vapor. *Exp. Fluids* **59** (8), 126.

THOL, M., DUBBERKE, F.H., BAUMHÖGGER, E., VRABEC, J. & SPAN, R. 2017 Speed of sound measurements and fundamental equations of state for octamethyltrisiloxane and decamethyltetrasiloxane. *J. Chem. Engng Data* **62** (9), 2633–2648.

THOMPSON, P.A. 1971*a* A fundamental derivative in gasdynamics. *Phys. Fluids* **14** (9), 1843–1849.

THOMPSON, P.A. 1971*b* *Compressible-Fluid Dynamics*. McGraw-Hill.

TOSTO, F., LETTIERI, C., PINI, M. & COLONNA, P. 2021 Dense-vapor effects in compressible internal flows. *Phys. Fluids* **33** (8), 086110.

TSIEN, H.-S. 1946 One-dimensional flows of a gas characterized by Vander Waal's equation of state. *J. Math. Phys.* **25** (1–4), 301–324.

VIMERCATI, D. & GUARDONE, A. 2018 On the numerical simulation of non-classical quasi-1D steady nozzle flows: capturing sonic shocks. *Appl. Maths Comput.* **319**, 617–632.

VIRTANEN, P., *et al.* 2020 SciPy 1.0: fundamental algorithms for scientific computing in Python. *Nat. Meth.* **17**, 261–272.

VOGEL, E., KÜCHENMEISTER, C. & BICH, E. 2000 Viscosity correlation for isobutane over wide ranges of the fluid region. *Intl J. Thermophys.* **21** (2), 343–356.

WAGNER, W. & PRUSS, A. 2002 The IAPWS formulation 1995 for the thermodynamic properties of ordinary water substance for general and scientific use. *J. Phys. Chem. Ref. Data* **31** (2), 387–535.

WILKE, C.R. 1950 A viscosity equation for gas mixtures. *J. Chem. Phys.* **18** (4), 517–519.

YEDDULA, S.R., GUZMÁN-IÑIGO, J. & MORGANS, A.S. 2022 A solution for the quasi-one-dimensional linearised Euler equations with heat transfer. *J. Fluid Mech.* **936**, R3.

YEOM, G.-S. & CHOI, J.-I. 2019 Efficient exact solution procedure for quasi-one-dimensional nozzle flows with stiffened-gas equation of state. *Intl J. Heat Mass Transfer* **137**, 523–533.

ZUCROW, M. 1976 *Gas Dynamics*. Wiley.